

Hydrodynamics of an Undulating Fin for a Wave-Like Locomotion System Design

Fangfang Liu, Kok-Meng Lee, *Fellow, IEEE*, and Can-Jun Yang

Abstract—Motivated by the interest to develop an agile, high-efficiency robotic fish for underwater applications where safe environment for data-acquisition without disturbing the surrounding during exploration is of particular concern, this paper presents computational and experimental results of a biologically inspired mechanical undulating fin. The findings offer intuitive insights for optimizing the design of a fin-based robotic fish that offers several advantages including low underwater acoustic noise, dexterous maneuverability, and better propulsion efficiency at low speeds. Specifically, this paper begins with the design of a robotic fish developed for experimental investigation and for validating computational hydrodynamic models of an undulating fin. A relatively complete computational model describing the hydrodynamics of an undulating fin is given for analyzing the effect of propagating wave motions on the forces acting on the fin surface. The 3-D unsteady fluid flow around the undulating fin has been numerically solved using computational fluid dynamics method. These numerically simulated pressure and velocity distributions acting on the undulating fin, which provide a basis to compute the forces acting on the undulating fin, have been experimentally validated by comparing the computed thrust against data measured on a prototype flexible-fin mechanism.

Index Terms—Biomimetic, computational fluid dynamics (CFD), hydrodynamic model, propulsion, robotic fish, undulating fin.

I. INTRODUCTION

INTERESTS to inspect submerged structures (such as boats, oil and gas pipes) and to detect environmental pollution and deep sea exploration have motivated researchers and scientists to develop bio-inspired concepts of underwater propulsion systems. Wave-like propulsion (that employs flexural waves similar to that used by stingrays, knifefish, or cuttlefish in nature) has recently been found experimentally feasible [1], [2]. In comparison with traditional propulsions (such as jets and axial propellers), wave-like systems offer several advantages including

low underwater acoustic noise, great maneuverability, and good propulsive efficiency at low speeds [3]. These advantages enable biomimetic wave-like locomotion systems to perform tasks (such as data acquisition) without disturbing the conditions of its surroundings. Developing a cost-effective wave-like locomotion system requires a good understanding of propulsion hydrodynamics, which also provides an essential basis for effective motion control of undulating fins.

Inspired by the morphological and functional features enabling a real fish to swim energy efficiently with speed and graceful maneuverability, a flurry of robotic devices has been developed to study mechanisms utilized by fish and other aquatic animals for designing artificial underwater systems (see examples, [4]–[9]). Research focuses span from motion control [10] and maneuvering [11], hydrodynamic simulation [12], and geometric optimization [13]. More recently, new smart materials (such as ionic polymer–metal composites and conjugated polymers) have been widely used to design aquatic microrobots [14]–[18] because they are flexible and produce significant bending deformation under low voltages [19]. For oceanic applications (such as collecting gas-tight samplers at seafloor [20]), there remains a need to develop payload-carrying wave-like locomotion systems capable of preserving its surroundings while performing underwater tasks.

Many biologically inspired robots have been recently proposed based on undulating-finned animals [21]–[23]. Methods employed to analyze propulsion hydrodynamics include analytical models [24], [25], and more recently numerical simulations [17], [26], [27] and experimental methods [16], [28]. In [16], the flow field generated by an ionic polymer–metal composite (IPMC) strip vibrating in a quiescent aqueous environment was investigated using planar particle image velocimetry (PIV). The results are useful for engineering bio-inspired vehicles with undulatory thrusters. Fish-like swimmers propelled by an IPMC are modeled and experimentally characterized in [18] and [19] where [18] incorporated IPMC actuation dynamics and the hydrodynamics to predict the steady-state cruising speed of the robot with a passive plastic fin attaching to the IPMC beam and [19] used rigid body dynamics to describe the vehicle motion considering the hydrodynamic effects and time-varying dynamics exerted by the vibrating IPMC on the body. Four undulating fin patterns in 2-D space were numerically analyzed in [21] using unsteady computational fluid dynamics (CFD) method for investigating the effect of pressure distributions on fin surface and thrust produced.

Motivated by the needs to analyze the undulating fin performance in designing a wave-like robotic fish, this paper offers the followings.

Manuscript received September 30, 2010; revised December 22, 2010; accepted January 11, 2011. Date of publication February 28, 2011; date of current version April 27, 2012. Recommended by Technical Editor G. Liu. This work was supported in part by the National Natural Science Foundation of China under Grant 50675198, in part by the Program for New Century Excellent Talents in University under Grant NCET-07-0756, in part by the Fundamental Research Funds for the Central Universities under Grant 2009QNA4003, and in part by the Zhejiang Provincial Natural Science Foundation of China under Grant R1090453.

F. Liu and C.-J. Yang are with the Institute of Mechatronics and Control Engineering, Zhejiang University, Hangzhou 310027, China (e-mail: fangfliu.zju@gmail.com; ycj@zju.edu.cn).

K.-M. Lee is with the George W. Woodruff School of Mechanical Engineering, Georgia Institute of Technology, Atlanta, GA 30332-0405 USA (e-mail: kokmeng.lee@me.gatech.edu).

Digital Object Identifier 10.1109/TMECH.2011.2107747

- 1) We present the hydrodynamic model of an undulating fin [2] which, unlike most robotic fins mimicking the pectoral fin of a fish, does not require individually actuated fin rays. With a single actuator, the undulating film propagates the wave in the opposite direction of the swim direction.
- 2) A prototype wave-like robotic fish has been designed and developed for experimental investigation and for validating computational hydrodynamic models of an undulating fin.
- 3) A relatively complete computational model describing the hydrodynamics of an undulating fin is given. Physical values of the geometric and kinematic parameters used in the computation have been based on the prototype flexible-fin mechanism so that numerical solutions can be validated experimentally.
- 4) The 3-D unsteady dynamics of the undulating fin has been numerically solved for the pressure and velocity distributions acting on the undulating film using the finite volume method (FVM), which provide the basis to compute the forces acting on the undulating fin.
- 5) Simulated results have been experimentally validated by comparing the average computed thrust against data measured on the prototype flexible-fin robotic fish. The results show that this analysis method is feasible and reasonable for analyzing the propulsion performance.

II. OVERVIEW OF THE ROBOTIC FISH SYSTEM

Fig. 1 shows the CAD model of the radio-controlled robotic fish consisting of three functional units: a mechanical fin for propulsion, a gravity allocation module for regulating depth, and a swing tail controlling the turning movement of the fish with a servomotor. Since the distance covered by radio communication is limited underwater, serial communication is used as a backup for controlling the robotic fish when it swims below certain depth.

A. Operational Principle

To illustrate the operational principle, the following describes two key components of the robotic fish: mechanical fin and gravity allocation module.

1) *Mechanical Fin*: The oscillating mechanical fin that propels the fish forward is driven by dc-motor actuated crank–slider mechanisms (located at the head) as schematically shown in Figs. 2 and 3. The motion plane y – z is perpendicular to the motor shaft (at point B) of the crank–slider mechanism. As the crank (with radius r) rotates with angular velocity ω , the link OA (where the flexible film is affixed) oscillates cyclically within an angular range $\pm\theta_m$ about the point O. In Fig. 2(b) where OB (with length h) is fixed, the vector sum $\mathbf{OB} + \mathbf{BC} = \mathbf{OC}$; hence, the angular displacement of the link OA is given as follows:

$$\theta = \begin{cases} \vartheta & \vartheta \geq 0 \\ \vartheta + \pi & \vartheta < 0 \end{cases} \quad (1a)$$

where

$$\vartheta = \tan^{-1} \frac{r \sin(\omega t)}{h + r \cos(\omega t)}. \quad (1b)$$

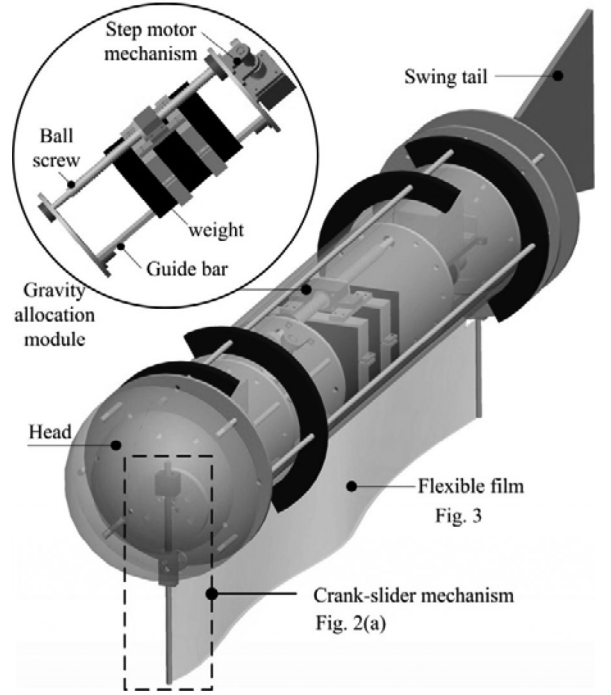


Fig. 1. 3-D CAD model of a robotic fish.

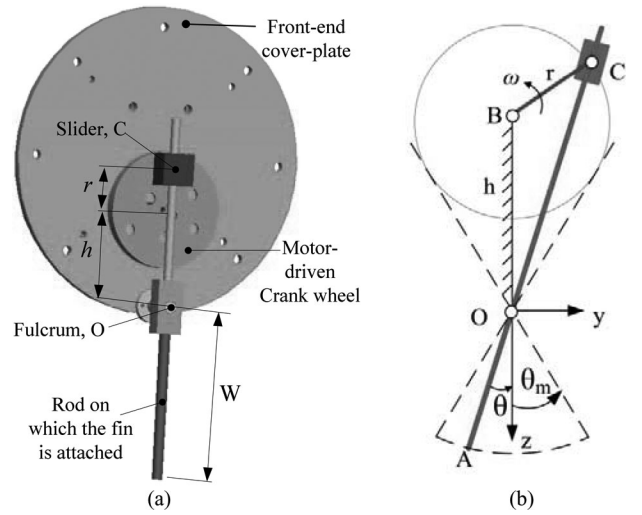


Fig. 2. Schematics illustrating driving mechanism of the mechanical fin. (a) Crank–slider mechanism. (b) Illustrating schematics.

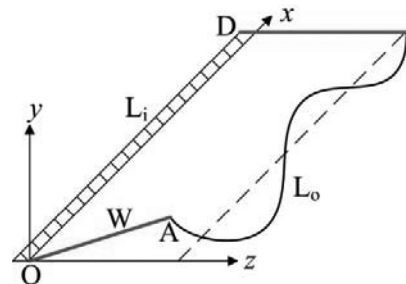


Fig. 3. Fin with flexible film.

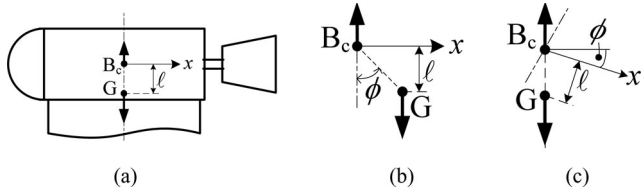


Fig. 4. Schematics illustrating pitching up movement. (a) Equilibrium. (b) cg closer to tail. (c) Pitch up.

As shown in Fig. 3, the inner side OD of the flexible film is fixed to the fish body. For clarity, the reference coordinate frame (origin O) is defined in Figs. 2(b) and 3, where the x -axis is along the fixed edge of the flexible film while the z -axis pointing downward along OB.

By actuating the head crank–slider to undulate the fin, a traveling wave can be generated passing from the head to tail producing the thrust that moves the fish forward. Similarly, the robotic fish can be controlled to swim backward if the tail crank–slider (not shown) is actuated with respect to its head mechanism. The generated sinusoidal waveform (with decaying amplitude along the x direction) is not arbitrary but depends on several factors (such as fin aspect ratio, material and thickness, and actuation design [29]); among these is the effect of propulsion frequency being explored in this paper. For a given mechanism and film material, different lengths of outer edges are able to generate different wave amplitudes (or number of waves).

2) *Gravity Allocation Module*: As shown in Fig. 1, the gravity allocation module consists of a moving weight that can be positioned by the motorized ball-screw/gear mechanism. The robotic fish has its center of gravity (cg) located ℓ mm vertically below its center of buoyancy when fully submerged horizontally in water (see Fig. 4a). In this equilibrium position, the weight is centered $x = L_i/2$ between the two end covers along the ball screw.

The pitch angle ϕ of the fish can be controlled by moving the weight along the ball screw. As illustrated in Fig. 4(b), if the weight is moved toward the tail ($x = L_i/2 + \ell \tan \phi$), the misalignment between the buoyancy and gravity would result in a clockwise moment causing the fish head to pitch up until the cg fish is $(\ell/\cos\phi)$ vertically below its center of buoyancy (see Fig. 4c). Similarly, when the weight is positioned at $x = L_i/2 - \ell \tan \phi$, the fish head pitches down to vertically balance the buoyancy force against gravity. Thus, by pitching the fish head up or down, the robotic fish can be controlled to dive in water by appropriately positioning the weight in the gravity allocation module while the undulating fin propels. Once reaching the specified depth, the weight is moved in the opposite direction returning to its horizontal equilibrium (where the cg and buoyancy center are vertically aligned) at the new depth. The gravity-based pitching mechanism is easy to implement and does not require additional static/dynamic seal.

B. Experimental Prototype

Fig. 5(a) shows an experimental prototype of the robotic fish developed at Zhejiang University [2], and its dimension is given in Fig. 5(b). The flexible film is a 0.2-mm-thick latex sheet with

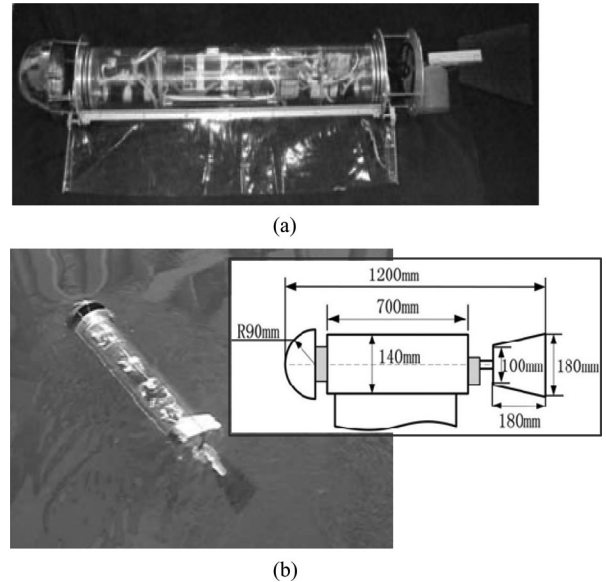


Fig. 5. Robotic fish developed at Zhejiang University [2]. (a) Prototype robotic fish. (b) Swimming horizontally forward, submerged in lake.

a trapezoidal shape ($L_i = 0.5$ m, $L_o/L_i = 1.36$, and $W = 0.15$ m). The initial weight and buoyancy of the robotic fish were 110 N and 125 N, respectively. Additional weights were placed in the robotic fish to balance the buoyancy and lower its cg when fully submerged in water. The fish cg is $\ell = 18$ mm below the center of buoyancy.

Underwater experiments showed that the appropriate frequency range for the prototype fish is $f = [2, 4]$ Hz; below 2 Hz the velocity of the undulating fin (relative to its surrounding fluid) is too low to generate a significant thrust. The thrust increases with propulsion frequency until $f = 4$ Hz, beyond which the system mechanically vibrates. The average propelling velocity U (computed by dividing the measured distance traveled by the fish by the time taken to complete the travel) at $f = 2, 3, 4$ Hz were found to be 0.17, 0.22, and 0.25 m/s, respectively. The corresponding Reynolds numbers ($Re = UL_i/\nu$ where ν is the kinematic viscosity of the fluid) are 1.0×10^5 , 1.2×10^5 , and 1.4×10^5 respectively; the flow is typically turbulent.

III. FORMULATION OF THE CFD ANALYSIS

To gain intuitive insights and establish a rational basis for investigating the effects of the fin design on the mechanical fish propulsion, the flow fields around the film and its changes during fin undulation are numerically analyzed. Without loss of generality, we consider the case where only the head crank–slider is actuated (and the tail end is fixed but parallel to OB) for the 3-D unsteady CFD numerical analysis of the flexible film.

The unsteady flow field (of the incompressible fluid) around the film is governed by the Navier–Stokes momentum equations and the equation of continuity

$$\rho \frac{D\mathbf{V}}{Dt} = \mathbf{F} - \nabla p + \mu \nabla^2 \mathbf{V} \quad (2a)$$

and

$$\nabla \cdot \mathbf{V} = 0 \quad (2b)$$

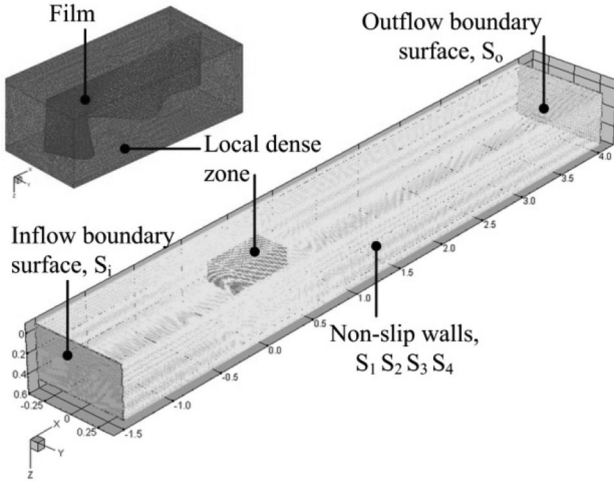


Fig. 6. Computational model of the flow field.

where ρ and μ are the density and dynamic viscosity of the fluid; \mathbf{V} is the fluid velocity vector; D/Dt is the total time derivative; \mathbf{F} is the body force acting on the fluid (primarily due to gravity); and p is the pressure.

A. Assumptions

Fig. 6 shows the computational model (for simulating the fluid flow passing through the flexible film within an open-ended rectangular channel with no-slip walls) where

$$x \in [-x_i, x_o], \quad y \in [-y_w, y_w], \quad z \in [-z_l, z_r]$$

where $x_i, x_o, y_w, z_l, z_r > 0$. The momentum equations are spatially discretized with a first-order upwind scheme while an implicit first-order scheme is used for temporal discretization (with time step size of 0.5 ms). The pressure/velocity coupling is handled through the continuity equation, using the semi-implicit method for pressure-linked equation (SIMPLE algorithm), valid for small time steps used in the simulation.

For solving the flow field using the FVM, the following assumptions are made.

- 1) The inflow passing through the upstream boundary surface

$$S_i(x = x_i, y = [-y_w, y_w], z = [-z_l, z_r])$$

is steady and uniform.

- 2) The downstream boundary surface

$$S_o(x = x_o, y = [-y_w, y_w], z = [-z_l, z_r])$$

is far from the flexible film. The outflow is steady, uniform, and equal to the inflow since the fluid is incompressible.

- 3) The four side-boundary surfaces (S_1, S_2, S_3, S_4) are also far from the flexible film such that the walls have little or no effects on the flow field around the flexible film.

B. Boundary/Initial Conditions

Based on the aforementioned assumptions, the boundary conditions essential to solve (2a,b) for a solution that is physically

relevant and initial conditions are specified as follows:

$$\text{at } S_i \text{ and } S_o, \quad V_x = U, \quad V_y = V_z = 0 \quad (3a)$$

$$\text{at } S_1, S_2, S_3, S_4, \quad \mathbf{V} = 0 \quad (3b)$$

$$\text{at } t = 0 \quad p = 0 \quad \text{and} \quad \mathbf{V} = 0. \quad (3c)$$

C. Input Parameters

To simulate the flow field around the flexible film, the mechanical motion of the flexible fin is specified as an input for a given design geometry. Previous experiments [29] suggest that the undulating fin motion (Fig. 3) has the following form:

$$y(x, z, t) = A(x, z) \sin \left[2\pi \left(\frac{x}{\lambda} - ft \right) \right] \quad (4)$$

where

$$A(x, z) = az(x + b).$$

In (4), $A(x, z)$ depicts the wave amplitude; λ and $f (= 1/T$ where T is the period) are the wavelength and frequency, respectively; (a, b) are constants to be experimentally determined.

D. Force Models

Once the pressure and velocity distributions are known, the hydrodynamic forces acting on the film surface (and hence the thrust of the robotic fish) due to the undulating motion can be calculated using the force models illustrated in Fig. 7, which shows the forces (thrust and drag force in the horizontal direction, and weight, buoyancy, and hydrodynamic lift in the vertical direction) acting on the robotic fish. The hydrodynamic stability and direction of the movements are often considered in terms of roll, yaw, and pitch. For understanding the sensitivity of fin design on propulsions, we focus here on the translational motion of the fish (mass m):

$$m \frac{d\mathbf{V}_f(t)}{dt} = \mathbf{F}_T(t) - \mathbf{F}_D(t) \quad (5)$$

where \mathbf{V}_f is the instantaneous velocity of the fish; and \mathbf{F}_T and \mathbf{F}_D are the corresponding thrust and drag force acting on the fish. The steady-state forces in the x direction at $F_T(t) = F_D(t)$ can be found from

$$F_T(t) = \int_S p(t) (\mathbf{n}_x \cdot d\mathbf{S}) \quad (6a)$$

$$F_D(t) = \mu \int_S \left(\frac{\partial v(t)}{\partial \delta} \cdot \mathbf{n}_x \right) |_{\delta=0} dS \quad (6b)$$

where $\partial v / \partial \delta$ is the normal velocity gradient in the boundary layer (or fluid layer in the immediate vicinity of the film or body surface where the effects of fluid viscosity are considered in detail) evaluated at the surface $\delta = 0$; \mathbf{n}_x is the unit vector in the x direction; and S is the wetted surface area of the film. In (6a), the stress vector $\mathbf{p}(t)$ acting on the propulsive element is almost normal to the surface of the element. For the range of $10^3 < Re < 5 \times 10^6$ (the condition in which fishes typically swim), the fluid inertia dominates as compared to its viscous forces implying that their resultant force F_{ri} acting on the i th propulsive element is primarily normal to its surface as shown

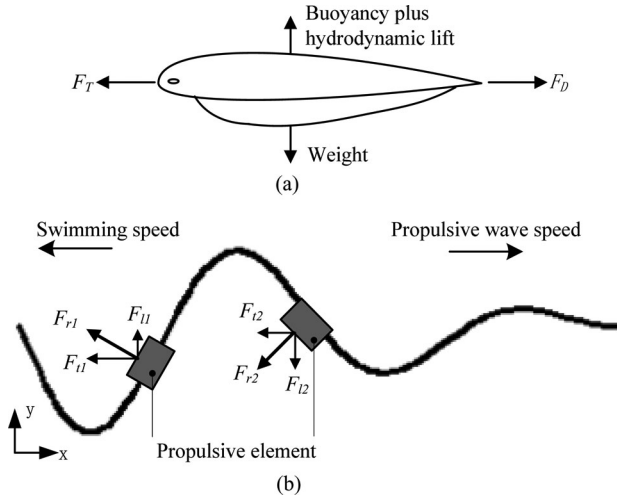


Fig. 7. Schematics illustrating the forces acting on a fish, adapted from [3]. (a) Hydrodynamic forces acting on a fish. (b) Elemental force on the fin.

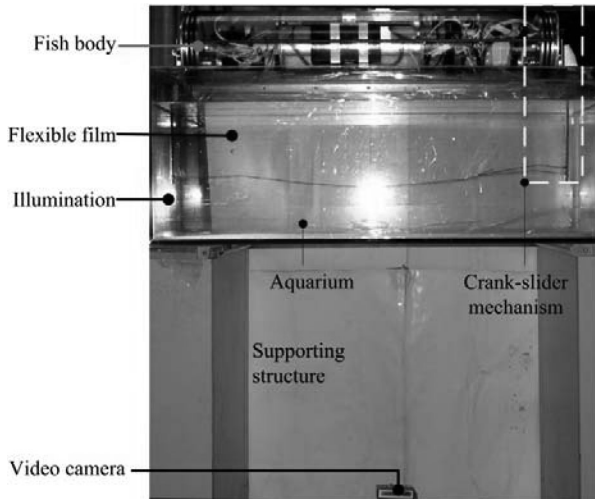


Fig. 8. Experimental setup.

in Fig. 7(b) where F_{ti} and F_{li} are the components in $-x$ and y directions, respectively.

E. Simulation Parameters

To specify the parameters (a, b, λ) in the wave equation (4) that describes the fin motion to solve the CFD model for the pressure and velocity fields (and hence the thrust and drag force acting on the fish), experiments were performed using the setup shown in Fig. 8, where the body of the robotic fish is placed on the top of the rectangular aquarium (0.80 m in length, 0.35 m in width, and 0.30 m in height); and the fin is completely immersed in water below. Each side of the aquarium is illuminated with a 1-kW lamp, and a Canon A620 camera is located below the aquarium filming (at a rate of 30 frames/s) the projected motion of the undulating flexible fin on the x - y plane. As a reference, square grids of 2 cm are graphed at the bottom of the aquarium to facilitate deriving the enveloping amplitude $A(x, z)$ that characterizes the wave equation (4) from the film.

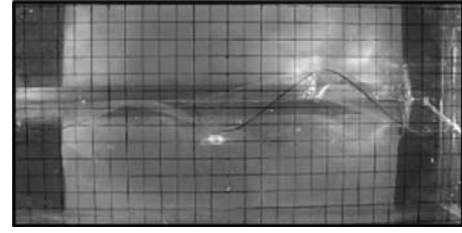


Fig. 9. Typical snapshot for characterizing the undulating fin.

TABLE I
FIN AND WAVEFORM PARAMETERS

Description	Parameter	Values
Fin length, m	L_i, L_o	0.5, 0.68
Fin width, m	W	0.15
Latex sheet, mm	Thickness	0.2
wetted surface area, m^2	S	0.75
Experimentally obtained $A(x, z)$:		
Propulsion frequency, Hz	F	2, 3, 4
Propulsion wavelength, m	λ	0.25
Envelop amplitude	(a, b)	$(-0.2, 0.5)$
Propelling velocity, m/s	U	0.17, 0.22, 0.25

A typical snapshot is shown in Fig. 9. Parameters characterizing the fin and its (experimentally found) motion amplitude are summarized in Table I. Propulsion wavelengths and envelope amplitudes may vary with propulsion frequency. However, negligible differences among data for the three different frequencies were observed experimentally; thus, the propulsion wavelength and envelop amplitude were assumed similar for the three frequencies (2, 3, and 4 Hz) in the subsequent simulations.

IV. RESULTS AND DISCUSSION

The pressure and velocity fields were numerically solved to provide insights into the effects of undulating fins on wave-like locomotion, and to validate the computational model against data obtained experimentally.

A. CFD Results

The FVM with an implicit segregated solver approach was employed to solve the 3-D unsteady fluid-flow equations (2a) and (2b) for the velocity V and pressure p around the fin for a specified propulsion frequency f . The model (2) with boundary and initial conditions (3) was solved using FLUENT, a commercial FVM package with a user-defined function (written and compiled in Visual C++) linked to the computational fin model to define its motion. Realizable κ - ϵ model was chosen for the turbulent model. The FVM simulations were based on experimentally obtained velocity values summarized in Table I.

The dimension of the computational region is $12L_i$ in length, $6W$ in width, and $6W$ in height, where L_i and W are defined in Fig. 3. The computational mesh consists of 952 378 tetrahedral elements around the film, and sparse hexahedral elements for the remainder of the domain. For reducing the computational time while not affecting the accuracy, the dynamic meshes are only updated in the vicinity of the undulating fin, which is referred

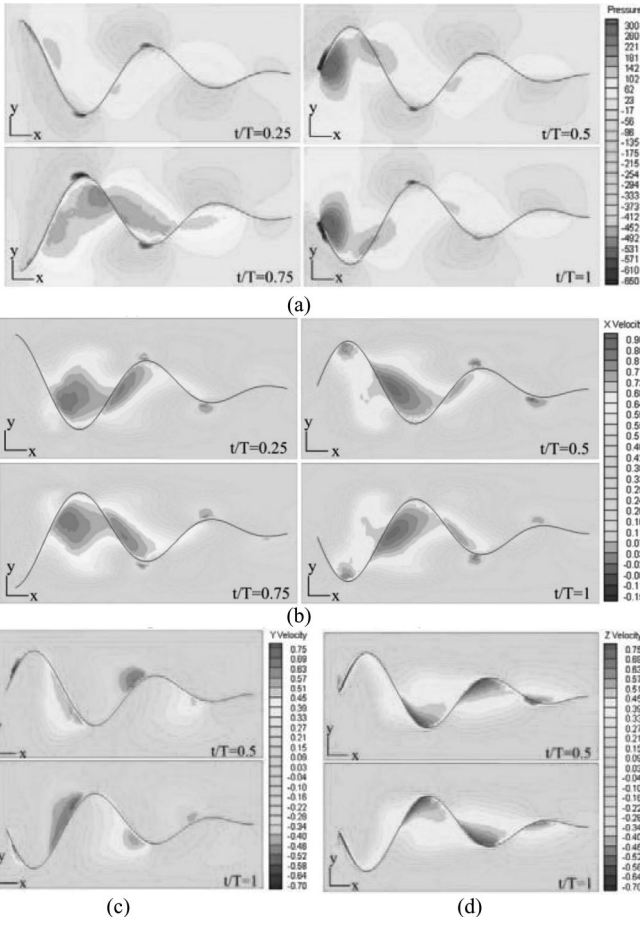


Fig. 10. Simulated CFD results at $f = 4$ Hz, $z = 0.15$ m. (a) Pressure distribution in Pa; $f = 4$ Hz, $z = 0.15$ m. (b) x -component velocity distribution (m/s); $f = 4$ Hz, $z = 0.15$ m. (c) y -component velocity (m/s). (d) z -component velocity (m/s).

to here as the local dense zone in Fig. 6. A static mesh is used for the remaining domain.

Simulated results at $f = 4$ Hz are presented in Fig. 10. Fig. 10(a) is four sequential snapshots (captured at $t/T = 0.25, 0.5, 0.75,$ and 1 where $T = 1/f = 0.25$ s is the period during an undulation cycle) showing the pressure distribution at $z = 0.15$ m (the outer side of the film). The corresponding velocity distributions around the film are given in Fig. 10(b)–(d). The effects of different frequencies on the pressure and velocity vectors at $z = 0.15$ m ($f = 2, 3$ Hz) are given in Fig. 11.

Some observations can be made from the computed pressure and velocity results.

- 1) 1) As the actuating link of the fin oscillates about the z -axis (see Fig. 2), the pressure and velocity distributions in Fig. 10(a) and (b), respectively, at $t/T = 0.75$ and 1 are mirror images of those at $t/T = 0.25$ and 0.5 as expected.
- 2) As shown in Fig. 10(a), regions of positive and negative pressure develop during the fin undulation, which generate a wave transmitting along the $+x$ direction. As a result, the film reacts to the positive fluid pressure around it in the $-x$ direction. Some negative pressure regions can be seen near the wave crests and troughs due to the change in the

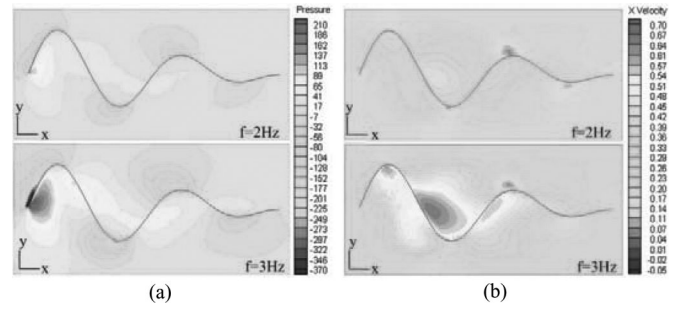


Fig. 11. Effect of frequency on p and V_x contours; $z = 0.15$ m, $t/T = 0.5$. (a) p contours in Pa. (b) V_x contours in m/s.

direction of the fin movement. Large pressure differences are generated across the film near the actuating end, and decrease along x because wave attenuates and loses energy.

- 3) Fig. 10(b) shows that the velocity of the fluid enveloped by the film is larger than that away from the film where the velocity U is steady and uniform. The reaction of the undulating film increases the fluid momentum enveloped by the film, which can be described as follows:

$$\frac{d}{dt}(m_w \mathbf{V}) \approx \mathbf{F}_w \quad (7)$$

where m_w is the mass of the fluid enveloped by the film and \mathbf{F}_w is the reaction acting on the fluid. Around the wave crest and trough, the x -component velocity of the fluid not enveloped by the film is nearly zero or negative corresponding to the pressure distribution.

- 4) As the fin undulation is symmetrical about the y -axis but asymmetrical about the z -axis, these have different influences on the instantaneous y - and z -components of the fluid velocity as compared between Fig. 10(c) and (d). The asymmetrical undulation about the z -axis generates a hydrodynamic lift, while the x -component velocity propels the robotic fish forward. This confirms the results observed in the flow visualization experiment in [2].
- 5) Fig. 11 shows that the pressure difference across the fin increases with propulsion frequency from approximately 260 Pa at 2 Hz to 950 Pa at 4 Hz. The x -component velocity difference enveloped by the film increases from about 0.55 m/s at 2 Hz to 1.05 m/s at 4 Hz. These findings show that the propulsive properties are dependent on frequencies, which are consistent with results observed in previous research [22] and the experimental results listed in Table III.

B. Verification and Validation

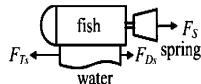
To verify the computational model against experimental data, the hydrodynamic forces acting on the film surface (and hence the thrust and drag force on the fish) due to the undulation motion were calculated from (6a) and (6b) using the computed pressure and velocity fields. In this study, the drag force $\mathbf{F}_D(t)$ acting on the body and on the undulating film were computed separately, which are denoted here as $\mathbf{F}_{Db}(t)$ and $\mathbf{F}_{Df}(t)$ respectively. To provide a basis for comparison between computational results

TABLE II
COMPUTED AVERAGE FORCES IN A CYCLE

Cases	Thrust and drag forces, (N)	Frequency, f (Hz)		
		2	3	4
Case 1: $U \neq 0$ Dynamically balanced	F_{Dbd}	1.67	2.65	3.28
	F_{Dfd}	0.07	0.13	0.19
	$F_D = F_{Dfd} + F_{Dbd}$	1.74	2.78	3.47
	F_{Td}	-1.85	-2.98	-3.78
	$\Delta F = 100\%(F_{Td} - F_D)/ F_{Td} $	5.95	6.71	8.20
Case 2: $U = 0$ Statically balanced	F_{Dfs}	0.10	0.19	0.25
	F_{Ts}	-1.56	-2.59	-3.13
	$F_s = -(F_{Ts} + F_{Dfs})$	1.46	2.4	2.88

TABLE III
EXPERIMENTAL RESULTS

F Hz	U m/s	$ F_s $ (N)		ΔF_s %
		Measured	Computed	
2	0.17	1.32	1.46	-10.6
3	0.22	2.00	2.40	-20.0
4	0.25	2.26	2.88	-26.8



and data obtained from underwater experiments, the following two cases are considered.

Case 1: Robotic fish swims with a constant velocity ($U \neq 0$).

When the robotic fish swims underwater at a constant U while the film undulates, the drag force is given by

$$\mathbf{F}_D|_{\text{constant } U} = \mathbf{F}_{Dfd} + \mathbf{F}_{Dbd} \quad (8)$$

where the subscript “ d ” denotes dynamical balance.

Case 2: Robotic fish undulates at a fixed position ($U = 0$).

Since the robotic fish body does not move in water and, thus, contributes no drag force

$$\mathbf{F}_D|_{U=0} = \mathbf{F}_{Dfs} \quad (9a)$$

and

$$\mathbf{F}_{Dbs} = 0 \quad (9b)$$

where the subscript “ s ” denotes static balance. This configuration is commonly used to experimentally determine the average thrust \mathbf{F}_T (generated by the undulating film of the robotic fish) by statically balancing the generated thrust against a measurable external force \mathbf{F}_s (such as a mechanical spring) and the drag force acting on the film

$$\mathbf{F}_{Ts} + \mathbf{F}_{Dfs} + \mathbf{F}_s = 0. \quad (10)$$

The force \mathbf{F}_s so measured is expected to be less than the thrust \mathbf{F}_{Ts} by amount equal to the drag force \mathbf{F}_{Dfs} acting on the film.

1) *Computed Forces:* The thrust F_T for both statically and dynamically balanced cases (at $f = 2, 3$, and 4 Hz) were calculated from (6) and graphed in Fig. 12(a) and (b), respectively, and their differences are given in Fig. 12(c). Other computed results averaged over one cycle are summarized in Table II. In Fig. 12 and Table II, the negative sign indicates that the thrust is in the opposite direction of positive x .

The computed results are analyzed as follows.

1) As shown in Fig. 12, the forces change periodically undergoing two cycles within their corresponding undulation

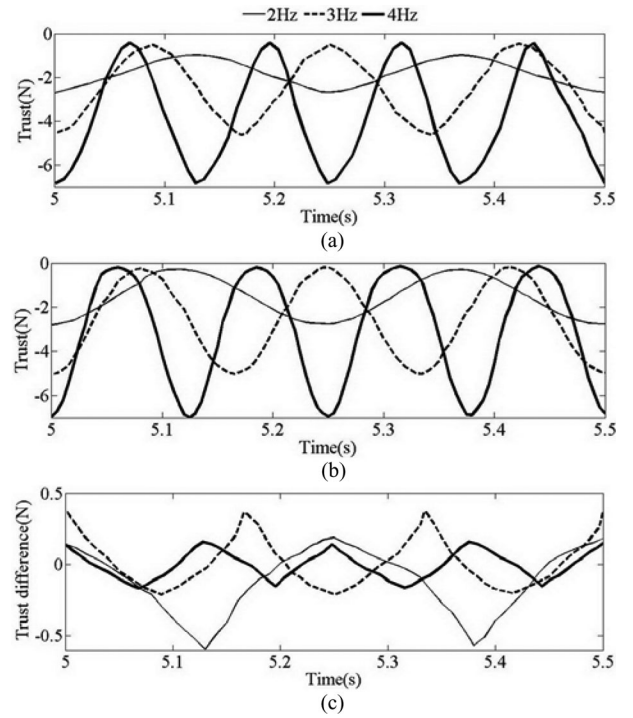


Fig. 12. Computed thrust forces as a function of time. (a) Dynamically balanced thrust F_{Td} (case 1). (b) Statically balanced thrust F_{Ts} (case 2). (c) Differences between cases 1 and 2.

cycles; the force has a period of half of the undulation cycle. The maximum values occur at $t_i/T_i = 0.5n$ ($i = 1, 2, 3$) where n is an arbitrary natural number and $i = 1, 2, 3$ indicates the frequency at 2, 3, or 4 Hz, respectively. These instants correspond to the largest velocity of the link OA (see Fig. 2) within a cycle, and are consistent with the large relative velocity of the enveloped fluid as observed in Fig. 10(b).

- 2) Theoretically, $F_T = F_D$ for a constant U as shown in (5). The drag forces on the body and film (F_{Dbd} and F_{Dfd}) were separately computed. The effect of velocity variation due to fin undulation on the body contributes to some discrepancy (between F_T and F_D); $\Delta F < 10\%$.
- 3) The fin kinematic pattern, which has a direct effect on the stresses $p(t)$ and hence on the thrust (6a), was obtained experimentally by anchoring the fish body. Its effect on the robotic fish moving at a constant U is examined here by comparing the thrust difference between the two (static and dynamical balance) cases in Fig. 12(c). The difference is very small (2.4%) at the operating frequency $f = 4$ Hz at which the parameters of fin kinematic pattern were experimentally obtained, but increases as the propulsion frequency departs from 4 Hz as expected; for example, the difference increases to 8.3% at 3 Hz and to 25% at 2 Hz.
- 2) *Experimental Data:* For validation, experiments were conducted in a large pool (20 m \times 20 m \times 1 m) to determine the average propelling velocity U and the force F_T in terms of propulsion frequency. For each propulsion frequency f setting, the radio-controlled robotic fish was fully submersed and

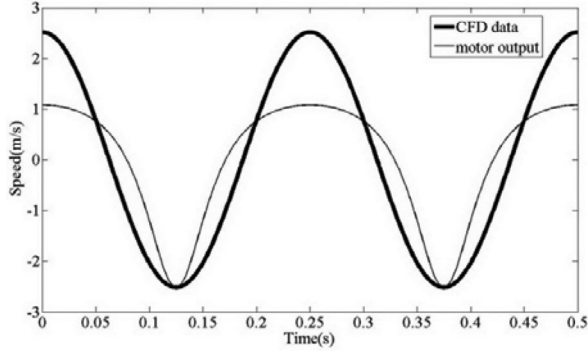


Fig. 13. Comparison two different speed profiles at tip A (see Fig. 2); speed derived from the derivative of (4) for the FVM simulation and from (12). $f = 4$ Hz.

balanced horizontally in water at a specified depth. The effective thrust force generated by the undulating fin was experimentally measured using the statically balanced configuration (Case 2), which statically balanced against an external spring force \mathbf{F}_s by attaching the tail to an extensible scale with a calibrated low spring constant of 8.6 N/m (Table III). The results are given in Table III, where

$$\Delta F_s = \frac{|F_s|_{\text{measured}} - |F_s|_{\text{computed}}}{|F_s|_{\text{measured}}} \times 100\%. \quad (11)$$

The differences between computed and experimentally measured $|F_s|$ are -10.6% , -20% , and -26.8% for 2, 3, and 4 Hz, respectively. Apart from the approximation in computing drag forces on the body and fin, which accounts for a significant portion of the difference, the neglected elastic deformation of the flexible film under the surrounding fluid pressure could also contribute to some discrepancy.

C. Effect of Crank–slider Design on Undulating Thrust

While the displacements of the undulating fin can be closely characterized from the motion images (see Figs. 8 and 9), the actual velocity of the fin undulation was found to be lower than the approximated sine function given by (4) used in the CFD simulation. To offer a better understanding, the angular velocity of OA actuated by the crank–slider mechanism is derived from the time derivative of (1b)

$$\frac{d\theta}{dt} = \omega \frac{\gamma \cos(\omega t) + 1}{\gamma^2 + 2\gamma \cos(\omega t) + 1} \quad \text{where} \quad \gamma = \frac{h}{r}. \quad (12)$$

The tangential speed v_e at tip A (see Fig. 2) is given by (12) multiplied by the moment arm W . Fig. 13 compares the speed derived from (4), where parameters were experimentally obtained data as inputs for the FVM simulation, against the speed v_e at tip A when the fin undulates at $f = 4$ Hz. Since the drag force F_D is proportional to the square of the velocity, the slightly overestimated thrust in simulation is consistent with the experimental data obtained using the actual robotic fish. From (12), $d\theta/dt \rightarrow \omega/2$ as $\gamma = h/r \rightarrow 1$ implying that (4) closely approximates the actual displacement and velocity at the tip A of the link OA when the crank–slider mechanism (see Fig. 2) is designed such that $h \rightarrow r$. As shown in Fig. 13, the

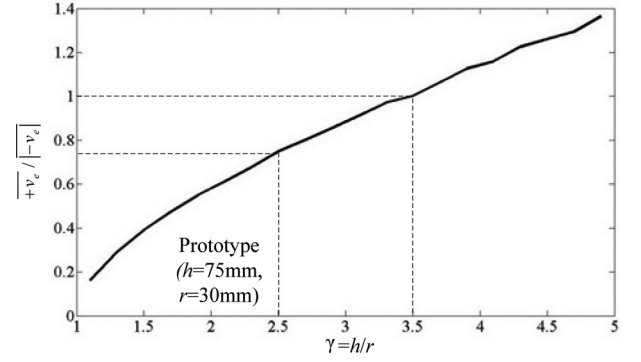


Fig. 14. Ratio $\overline{+v_e}/\overline{|-v_e|}$ as a function of γ at 4 Hz.

crank–slider mechanism has a quick-return feature, and its link OA has different forward and backward speeds.

The asymmetrical speed about the x - z plane could lead to an asymmetrical lateral force resulting in some yaw movement, which must be compensated by appropriately controlling the swing tail. For the existing prototype (where $r = 30$ mm and $h = 75$ mm), slight yaw movement as a result of the asymmetrical speed about x - z plane (thus, an asymmetrical lateral force) can be observed experimentally. The effect of asymmetrical velocity profile can be illustrated in Fig. 14, where the ratios of positive to negative speeds (averaged over one cycle) are plotted as a function of $\gamma = h/r$. The plot shows that the negative portion has a larger speed than the positive portion when h/r is less than 3.5 at which the ratio of positive to negative speeds is equal to 1, and thus, the net effect of the lateral force due to asymmetrical speed can be minimized.

V. CONCLUSION

A fin-based robotic fish has been presented. Along with a relatively complete numerical model for simulating the pressure and velocity fields around the undulating fin, underwater experiments were performed to determine the parametric values to describe the undulating fin motion in simulations, and to validate the computational model. The computational model has been experimentally verified by comparing the computed thrust against measured data, which agree well. The findings provide a rationale basis for investigating the effect of fluid flow field around the mechanical fin on propulsive performance. The results, as observed from the flow visualization in [2] and CFD simulations, confirm that asymmetrical undulation about the z -axis generates a hydrodynamic lift while the x -component velocity propels the robotic fish forward. This asymmetrical hydrodynamic lift, however, can be eliminated in a dual-fin design employing a pair of symmetric fins commonly seen in fish such as stingray and cuttlefish. The crank–slider design has an effect on the asymmetrical lateral force that could lead to some yaw movement requiring compensation by appropriately controlling the swing tail.

ACKNOWLEDGMENT

The authors thank J.-H. Zheng for technical help in developing the robotic fish.

REFERENCES

- [1] V. V. Krylov and G. V. Pritchard, "Experimental confirmation of the propulsion of marine vessels employing guided flexural waves in attached elastic fins," *J. Fluid. Struct.*, vol. 23, pp. 297–307, 2007.
- [2] F. Liu, C.-J. Yang, and K.-M. Lee, "Hydrodynamic modeling of an undulating fin for robotic fish design," in *Proc. IEEE/ASME Int. Conf. Adv. Intell. Mechatron. (AIM'10)*, Montréal, QC, Canada, pp. 55–60.
- [3] M. Sfakiotakis, D. M. Lane, and J. B. C. Davies, "Review of fish swimming modes for aquatic locomotion," *IEEE J. Oceanic Eng.*, vol. 24, no. 2, pp. 237–252, Apr. 1999.
- [4] S. Guo, T. Fukuda, and K. Asaka, "A new type of fish-like underwater microrobot," *IEEE/ASME Trans. Mechatronics*, vol. 8, no. 1, pp. 136–141, Mar. 2003.
- [5] M. G. Borgen, G. N. Washington, and G. L. Kinzel, "Design and evolution of a piezoelectrically actuated miniature swimming vehicle," *IEEE/ASME Trans. Mechatronics*, vol. 8, no. 1, pp. 66–76, Mar. 2003.
- [6] J. E. Colgate and K. M. Lynch, "Mechanics and control of swimming: A review," *IEEE Trans. Ocean. Eng.*, vol. 29, no. 3, pp. 660–673, Jul. 2004.
- [7] S. D. Kelly and R. B. Hukkeri, "Mechanics, dynamics, and control of a single-input aquatic vehicle with variable coefficient of lift," *IEEE Trans. Robot.*, vol. 22, no. 6, pp. 1254–1264, Dec. 2006.
- [8] G. V. Lauder, E. J. Anderson, J. Tangorra, and P. G. A. Madden, "Fish biorobotics: Kinematics and hydrodynamics of self-propulsion," *J. Exp. Biol.*, vol. 210, pp. 2767–2780, 2007.
- [9] F. Boyer, M. Porez, A. Leroyer, and M. Visonneau, "Fast dynamics of an eel-like robot-comparisons with Navier–Stokes simulations," *IEEE Trans. Robot.*, vol. 24, no. 6, pp. 1274–1288, Dec. 2008.
- [10] M. Narasimhan and S. N. Singh, "Adaptive input–output feedback linearizing yaw plane control of BAUV using dorsal fin," *Ocean Eng.*, vol. 33, pp. 1413–1430, 2006.
- [11] J. Yu, L. Liu, L. Wang, M. Tan, and D. Xu, "Turning control of a multilink biomimetic robotic fish," *IEEE Trans. Robot.*, vol. 24, no. 1, pp. 201–206, Feb. 2008.
- [12] S. Kern and P. Koumoutsakos, "Simulations of optimized anguilliform swimming," *J. Exp. Biol.*, vol. 209, pp. 4841–4857, 2006.
- [13] J. Yu, L. Wang, and M. Tan, "Geometric optimization of relative link lengths for biomimetic robotic fish," *IEEE Trans. Robot.*, vol. 23, no. 2, pp. 382–386, Apr. 2007.
- [14] Z. Chen and X. Tan, "A control-oriented and physics-based model for ionic polymer-metal composite actuators," *IEEE/ASME Trans. Mechatronics*, vol. 13, no. 5, pp. 519–529, Oct. 2008.
- [15] Y. Zhang, M. Cong, D. Guo, and D. Wang, "Design optimization of a bidirectional microswimming robot using giant magnetostrictive thin films," *IEEE/ASME Trans. Mechatronics*, vol. 14, no. 4, pp. 493–503, Aug. 2009.
- [16] S. D. Peterson, M. Porfiri, and A. Rovardi, "A particle image velocimetry study of vibrating ionic polymer metal composites in aqueous environments," *IEEE/ASME Trans. Mechatronics*, vol. 14, no. 4, pp. 474–483, Aug. 2009.
- [17] K. Abdelnour, E. Mancina, S. D. Peterson, and M. Porfiri, "Hydrodynamics of underwater propulsors based on ionic polymer metal composites: A numerical study," *Smart Mater. Struct.*, vol. 18, no. 8, pp. 1–11, 2009.
- [18] Z. Chen, S. Shatara, and X. Tan, "Modeling of biomimetic robotic fish propelled by an ionic polymer–metal composite caudal fin," *IEEE/ASME Trans. Mechatronics*, vol. 15, no. 3, pp. 448–459, Jun. 2010.
- [19] M. Aureli, V. Kopman, and M. Porfiri, "Free-locomotion of underwater vehicles actuated by ionic polymer metal composites," *IEEE/ASME Trans. Mechatronics*, vol. 15, no. 4, pp. 603–614, Aug. 2010.
- [20] Y. Chen, S. Wu, Y. Xie, C. Yang, and J. Zhang, "A novel mechanical gas-tight sampler for hydrothermal fluids," *IEEE J. Oceanic Eng.*, vol. 32, no. 3, pp. 603–608, Jul. 2007.
- [21] Y. Zhang, L. B. Jia, S. W. Zhang, J. Yang, and K. H. Low, "Computational research on modular undulating fin for biorobotic underwater propulsor," *J. Bio. Eng.*, vol. 4, pp. 25–32, 2007.
- [22] A. A. Shirgaonkar, O. M. Curet, N. A. Patankar, and M. A. MacIver, "The hydrodynamics of ribbon-fin propulsion during impulsive motion," *J. Exp. Biol.*, vol. 211, pp. 3490–3503, 2008.
- [23] T. Hu, L. Shen, L. Lin, and H. Xu, "Biological inspirations, kinematics modeling, mechanism design, and experiments on an undulating robotic fin inspired by *Gymnarchus niloticus*," *Mechanism Mach. Theory*, vol. 44, pp. 633–645, 2009.
- [24] M. J. Lighthill, "Large-amplitude elongated-body theory of fish locomotion," *Proc. R. Soc. Lond. B*, vol. 179, pp. 125–138, 1971.
- [25] T. Y. Wu, "Mathematical biofluid dynamics and mechanophysiology of fish locomotion," *Math. Methods Appl. Sci.*, vol. 24, pp. 1541–1564, 2001.
- [26] R. Mittal, "Computational modeling in biohydrodynamics: Trends, challenges, and recent advances," *IEEE J. Oceanic Eng.*, vol. 29, no. 3, pp. 595–604, Jul. 2004.
- [27] H. Suzuki and N. Kato, "A numerical study on unsteady flow around a mechanical pectoral fin," *Int. J. Offshore Polar Eng.*, vol. 15, no. 3, pp. 161–167, 2005.
- [28] J. Peng, J. O. Dabiri, P. G. Madden, and G. V. Lauder, "Non-invasive measurement of instantaneous forces during aquatic locomotion: A case study of the bluegill sunfish pectoral fin," *J. Exp. Biol.*, vol. 210, pp. 685–698, 2007.
- [29] F. F. Liu, C. J. Yang, Y. Q. Xie, and Y. Yang, "Initial development and experiments on a robotic fish with a novel undulating fin," in *Proc. 2008 IEEE Conf. Robot. Autom. Mechatronics*, Chengdu, China, 2008, pp. 1075–1078.



Fangfang Liu received the B.Eng. degree in 2006 from the Department of Mechanical Engineering, Zhejiang University, Hangzhou, China, where she is currently working toward the Ph.D. degree.

Her current research interests include development and hydrodynamics of biomimetic underwater robots.



Kok-Meng Lee (M'89–SM'02–F'05) received the B.S. degree from the State University of New York, Buffalo, in 1980, and the S.M. and Ph.D. degrees from the Massachusetts Institute of Technology, Cambridge, in 1982 and 1985, respectively.

Currently, he is a Professor in the Woodruff School of Mechanical Engineering at the Georgia Institute of Technology, Atlanta. His research interests include system dynamics/control, robotics, automation, and mechatronics. He holds eight patents in machine vision, three degrees of freedom (DOF) spherical motor/encoder, and live-bird handling system.

Dr. Lee is a Fellow of the American Society of Mechanical Engineers (ASME). He received the National Science Foundation (NSF) Presidential Young Investigator, Sigma Xi Junior Faculty Research, International Hall of Fame New Technology, and Kayamori Best Paper awards.



Can-Jun Yang received the B.Eng. degree and the M.Eng. degree from Nanjing University of Aeronautics and Astronautics, Nanjing, China, in 1991 and 1994, respectively, and the Ph.D. degree from Zhejiang University, Hangzhou, China, in 1997.

Since 1997, he has been with Zhejiang University, where he is currently a Professor and the Vice-Director of the Institute of Mechatronic and Control Engineering, and a member of the National Industrial Technological Innovation Union Council for Rehabilitation Technical Aids. His current research interests

include man–machine intelligent mechatronic system and deep-sea mechatronic equipment techniques.

Prof. Yang received the 2nd Prize of the National Award for Technical Invention in 2009.